optica

Epsilon-near-zero Al-doped ZnO for ultrafast switching at telecom wavelengths outpacing the traditional amplitude-bandwidth trade-off: supplementary material

N. KINSEY,[1] C. DEVAULT,[2] J. KIM,[1] M. FERRERA,[1,3] V.M. SHALAEV,[1] AND A. BOLTASSEVA[1,*]

[1] School of Electrical and Computer Engineering and Birck Nanotechnology Center, Purdue University, West Lafayette, Indiana 47907, USA
[2] Department of Physics and Birck Nanotechnology Center, Purdue University, West Lafayette, Indiana 47907, USA
[3] School of Engineering and Physical Sciences, Heriot-Watt University, Edinburgh, Scotland EH14 4AS, UK
*Corresponding author: aeb@purdue.edu

This document provides supplementary information to "Epsilon-near-zero Al-doped ZnO for ultrafast switching at telecom wavelengths outpacing the traditional amplitude-bandwidth trade-off," http://dx.doi.org/10.1364/optica.2.000616. A detailed discussion of a hybrid plasmonic modulator using aluminum doped zinc oxide as the dynamic material and the waveguide-modulator optimization procedure is presented, along with additional information on the growth and extraction of the optical properties of the unique oxygen-deprived aluminum doped zinc oxide films, the numerical model used to the fit experimental results, the pump-probe data fitting procedure, and titanium nitride thin film deposition and characterization methods.

1. INTEGRATED ALL-OPTICAL PLASMONIC MODULATOR

As a demonstration of the applicability and versatility of our as-grown AZO films, a simple plasmonic modulator is proposed which enables all-optical control of the signal amplitude at ultrafast rates. All-optical plasmonic devices promise extremely fast operational speeds in excess of 1 THz, beyond what is currently attainable with electronics or electro-optic hybrid devices. This increase in bandwidth is crucial for continuing the improvement and development of future all-optical communication networks. Additionally, the plasmonic nature of the device provides further advantages such as polarization purity, enhanced light-matter interaction, extreme sensitivity to changes in the guiding environment, support for both electrical and optical signals, and increased nonlinearities due to high field confinement. It is for these reasons that we focus on a plasmonic modulator design, although many outstanding examples of all-optical and optoelectronic modulation have been demonstrated in silicon photonic waveguides, semiconductor optical amplifiers, and polymer waveguides among others, but these strategies will not be discussed in this manuscript [1-14].

Many different materials and methods have been suggested to generate the desired temporal dependence such as material phase/structural changes [1, 15, 16], thermo‑optic effects [17], phase shifting through carrier injection [18, 19], nonlinearities [3, 9], and electro‑absorption [4, 6, 10, 20]. While some of these devices have been shown to achieve operational speeds greater than 10 GHz with appreciable modulation, for many modulators there is still a trade‑off between the speed and modulation depth [21]. More recently, transparent conducting oxides (TCOs) have received attention for their tunability, leading to several devices with some of the highest reported performance [22-26]. For more information on TCO based modulators see the following reviews and references therein [21, 27].
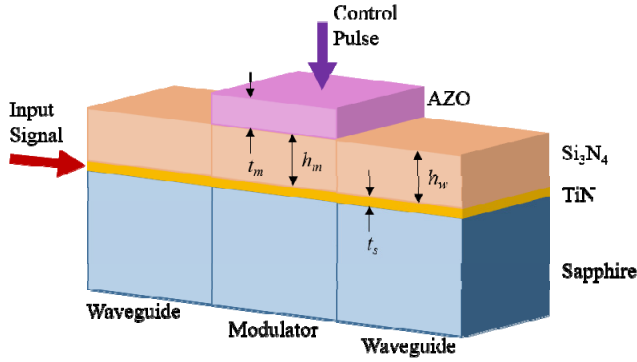
Fig. S1. Schematic of the as-grown AZO plasmonic modulator. The height of the silicon nitride cladding in the waveguide (h_w) was optimized using eigenmode analysis and set at 285 nm. The thickness of the TiN strip (t_s) is 7 nm for the entire structure. The thickness of the silicon nitride cladding for the modulator (h_m) is slightly larger than the waveguide (set to 315 nm) to account for the lower index of the AZO layer as opposed to air. The AZO layer (t_m) is set at 350 nm thick.

Fig. S2. a) Vertical mode cutline in the waveguide for the on and off-states. These curves overlap. b) Vertical mode cutline in the modulator for the on and off-states, illustrating the shift from a plasmonic mode to a photonic mode (i.e. not supported). c) Power flow in the structure along the direction of propagation. The modulator section is highlighted in red.

The proposed modulator structure is based from a hybrid plasmonic waveguide design using TiN and silicon nitride, shown to achieve low-loss propagation at 1.55 μm [28]. Such materials are largely beneficial for switching applications due to their CMOS-compatibility which provides a reliable and cheap standard to manufacture devices, enabling significant cost reduction and large-scale installations possible (i.e. in data centers). By using a waveguide as the base structure, the insertion loss into the device is minimized, allowing for many devices to be cascaded while maintaining appreciable throughput. A schematic of the modulator, coupled to an input and output waveguide, is illustrated in Fig. S1. A plasmonic wave is injected into the structure from the left and a control pulse is used to modify the permittivity of the as-grown AZO sample from the top. This results in two simultaneous effects: 1) The as-grown AZO has a stronger absorption and 2) The careful balance of the effective index is perturbed. Increased absorption clearly leads to a reduction of the signal, but during modulation there is also a mismatch in the modes supported within the two structures which leads a to larger insertion loss. This is of course desired in the on-state (i.e. high loss state), but decreases the performance in the off-state.

As a first-order optimization of the structure, the silicon nitride thickness h_w should be selected to minimize propagation losses in the waveguide and the thickness h_m should be selected such that the wavevector of the mode in the modulator is close to that in the waveguide (see following section). For an operating wavelength of 1.3 μm, the entire modulator structure was simulated in 2-D from the side so that propagation through both the connecting waveguides and the modulator stack could be analyzed. The optical pumping was simulated by simply altering the carrier concentration of the as-grown AZO film in a manner which corresponds to the values extracted from the pump-probe experiments (an incident fluence of 0 and 3.9 mJ/cm² was assumed). A 7 nm thick TiN strip with permittivity ε = -49 + i16 (as obtained from spectroscopic ellipsometry, see Supplementary Information) is used with a sapphire (n = 1.75) substrate and silicon nitride (n = 2) cladding. Vertical cut lines of the mode inside the waveguide Fig. S2(a) and modulator S2(b) are depicted for the on and off-state as well as the signal power as a function of the propagation distance in Fig. S2(c) (modulator length is highlighted in red).

Although subtle due to the selection of the modulator's geometry, the mode in the off-state is plasmonic, as an exponential decay in the substrate (z < 0) is evident near the metal (z = 0). Note that the profile in the silicon nitride (z > 0) is always Gaussian, resulting in the hybrid plasmonic-photonic nature of the waveguide [28, 29]. However, once pumped, the delicate index balance is no longer present and the mode
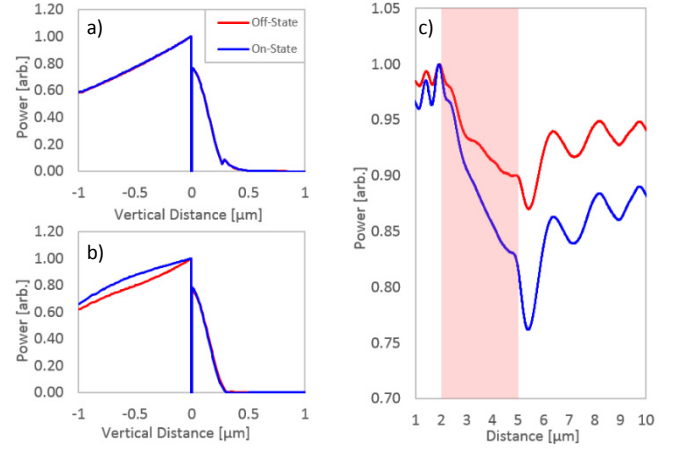
exhibits an almost fully Gaussian profile (Fig. S4(b) on-state). This is largely due to the fact that the plasmonic mode is significantly smaller in size within the biased modulator structure (i.e. low coupling coefficient) and the light has scattered to an available photonic mode. Although, this does provide efficient modulation, the scattered photonic modes can re-couple to the waveguide on the output side of the device (see slow increase of power for distances greater than 7 μm), thereby decreasing the modulation achieved. The beating noted in the output is due to an interference between the energy in the plasmonic mode and photonic modes of the structure. The mode recoupling and interference can be limited through the addition of absorbing layers below the device to prevent the scattered light from recoupling. As a result of the index mismatch and the increase in the absorption of the as-grown AZO, a maximum signal modulation depth of 0.4 dB/μm (extinction ratio of 0.2 dB/μm) is achieved, defined between the minimum and maximum of the power flow. The total insertion losses in the structure are 0.2 dB for the 10 μm section shown here, or 0.02 dB/μm, which is the result of a low off-state propagation loss and an optimal mode overlap between the waveguide and modulator. In addition, further optimization of the structure, namely the initial permittivity of the as-grown AZO layer, can lead to increased performance which is expected to approach an extinction ratio of 1 dB/μm without sacrificing insertion loss or speed.

Table S1. Performance comparison of all-optical plasmonic modulators.

Pump Energy	Speed	Insertion Loss [dB]	ER [dB]	FoM [W⁻¹]	Ref.
16 pJ	**2 ps**	**0.5**	**13.1**	**8.9×10^{23}**	**[30]**
625 pJ	**2 ps**	**0.5**	**4.8**	**8.0×10^{21}**	**[31]**
1.2 nJ	**352 fs**	**0.2**	**0.2**	**2.4×10^{21}**	**AZO**
91 nJ	200 fs	4.3	0.3	4.3×10^{18}	[3]
118 nJ	60 ps	4.6	10.5	3.2×10^{17}	[32]
7.2 nJ	10 s	17.4	0.8	6.2×10^{5}	[33]

To compare the performance of our device with previous works in literature for all-optical plasmonic modulators, a figure or merit has been defined as $FoM = (ER/\alpha)(1/E\tau)$ where ER is the extinction ratio (defined as $\alpha_{on} - \alpha_{off}$), α is the off-state loss, τ is the device recovery time, and E is the pumping energy. This FoM highlights the benefit-to-cost ratio of modulation depth to insertion loss as well as bandwidth to energy. The results of the AZO modulator presented here, along with several additional works in literature are shown in Table S1. For our device, a modulation area (as viewed from the top in Fig. S3) of 10 μm
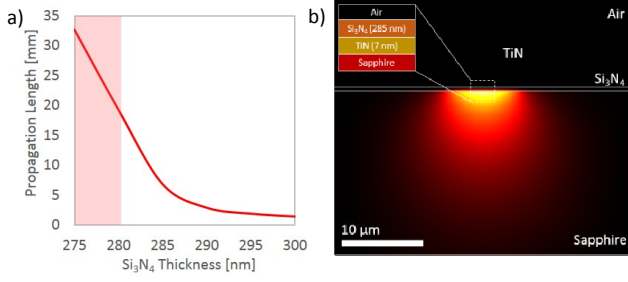
Fig. S3 a) Propagation length of the waveguide plasmonic mode versus the silicon nitride cladding thickness. The shaded region are modes with a photonic nature and are not considered in this analysis. b) Mode profile of the hybrid plasmonic mode in the waveguide for a silicon nitride thickness of 285 nm.
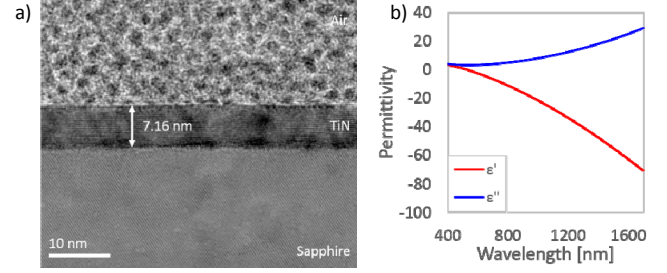

Fig. S4. a) TEM image of 7 nm thick TiN layer on c-sapphire. The cubic structure of TiN is evident due to the epitaxial growth on sapphire. b) Linear optical properties of TiN as extracted from spectroscopic ellipsometry measurements.

wide by 3 μm long is considered, as these dimensions are in line with our previous works on TiN waveguides. Consequently, a pulse energy of 1.2 nJ is required to achieve the fluence of 3.9 mJ/cm^2 used in our experiments, in-line with previously reported values of fluence and pulse energy for other plasmonic modulators [28]. For clarity, the three highest figures of merit have been bolded where the device presented here achieves the third highest performance. Among these devices, our structure achieves the fastest recovery speed by nearly an order of magnitude. Additionally, it should be noted that for several of the devices listed below, the insertion loss does not include coupling losses of the structure which can be quite significant for devices using gratings as in references [3, 31-33]. The inclusion of these extra losses can have a great effect on the final performance of the device since the coupling loss can easily be a few dB per facet.

In addition, the AZO-based modulator design uses CMOS-compatible materials. Among the works reported in Table S1, only the device of K. F. MacDonald *et al.* is also CMOS-compatible [3]. The meal-insulator-semiconductor-insulator-metal ring resonator proposed in reference [30] could be made CMOS-compatible by replacing silver with another metal, although the performance of the structure is likely to be reduced. Finally, we note that the performance of our device offers several areas for improvement enabling the device to be even more competitive such as a further reduction in size to limit energy requirements, an optimization of the as-grown AZO base permittivity, and the movement to high-index claddings to increase modal interaction with the active layer, to name a few.

Unlike many other all-optical modulators, the design presented here is shown to be simple (requiring just two standard photolithography steps) yet effective, achieving speeds consistent with even the fastest nonlinear all-optical modulators, and orders of magnitude faster than other methods [15, 17]). Consequently, this alternative material plasmonic modulator, powered by the tunability of the as-grown AZO, represents a viable device for future high-performance all-optical circuits.

2. PLASMONIC MODULATOR OPTIMIZATION

A first order optimization of the plasmonic modulator structure was completed by ensuring an ideal mode overlap between the waveguide and modulator structures. This was achieved using eigenmode analysis in COMSOL Multiphysics by sweeping the thickness of the cladding and observing propagation constants. The waveguide propagation loss versus silicon nitride thickness for a 7 nm thick TiN strip is shown Fig. S3 along with a mode profile. For thicknesses less than 280 nm (shaded in red in Fig. S3), the mode was photonic in nature, having its peak in the substrate and not near the metal's surface. These modes are not considered in this analysis, and correspondingly a silicon nitride thickness of 285 nm was chosen for the waveguide. This mode had a wavevector k_{spp} = 8.4579 × 10^6 - 74.44i (a propagation length more than 6 mm for a mode size of 3.5 μm). The same analysis was repeated for the modulator stack with

a 350 nm layer of AZO (base permittivity ε = 0.22 + i0.26) on top of the silicon nitride, and the height h_m was chosen to most closely match the k of the waveguide mode – a thickness of 315 nm. This ensures that in the off-state, the plasmonic mode is supported in both structures and minimizes the insertion loss.

3. OXYGEN-DEPRIVED AZO DEPOSITION AND CHARACTERIZATION

Aluminum-doped ZnO (AZO) films were deposited by pulsed laser deposition (PVD Products Inc.) using a KrF excimer laser (Lambda Physik GmbH) operating at a wavelength of 248 nm for source material ablation. A 2wt% doped AZO target was purchased from the Kurt J. Lesker Corp. with a purity of 99.99% or higher [34]. The energy density of the laser beam at the target surface was maintained at 1.5 J/cm^2 and deposition temperature was 75°C. We maintained the oxygen pressure under 0.01 mTorr to achieve additional free carrier from the oxygen vacancies. The prepared thin films were characterized by spectroscopic ellipsometry (J. A. Woollam Co. Inc.) in the spectral region from 300 - 2500 nm. The dielectric function of the films was retrieved by fitting a Drude (when ω_0 = 0) and Lorentz oscillator model (Eq. S1) to the ellipsometry data. To probe the electrical properties of thin films such as mobility and carrier concentration, we carried out the hall measurement (MMR Technologies) at the room temperature.

$$\varepsilon = \varepsilon_\infty + \sum \frac{\omega_p^2}{(\omega_o^2 - \omega^2) - i\omega\Gamma} \tag{S1}$$

4. TiN DEPOSITION AND CHARACTERIZATION

TiN is deposited using reactive magnetron sputtering in a nitrogen/argon environment (PVD Products Inc.) [35]. The substrate temperature is set to 800°C during deposition to obtain more metallic properties. The linear optical properties of TiN used in modeling the plasmonic modulator are derived from spectroscopic ellipsometry (J. A. Woollam Co. Inc.) where the thickness is determined from TEM (see Fig. S4(a)). A Drude + Lorentz model (Eq. S1) with one Lorentz oscillator and two Drude terms (i.e. ω_0 = 0) is used to fit the data. The extracted linear optical properties of the 7 nm thick TiN layer are shown in Fig. S4(b).

5. EXPERIMENTAL SETUP AND METHODS

An amplitude Ti:sapphire laser system (Spectra Physics) was used as the excitation source for this experiment, producing pulses of ~120 fs at 1 kHz and 800 nm. The output was then fed through an optical parametric amplifier (TOPAS Inc.) and set to an output of 650 nm. In our system, 650 nm is generated as the second harmonic (SH) of 1300 nm, and therefore both the 1300 nm and 650 nm beams exit the system collinearly. These beams were then guided to our experiment and separated using a dielectric mirror with high reflectivity above

1060 nm. The 1300 nm beam is first filtered to remove any residual 650 nm light and guided through a retroreflector placed on a computer controlled stage, providing a delay line. To generate the pump beam, the 650 nm beam was focused into a BBO crystal properly oriented to phase match the SH. Any residual 650 nm was removed with a short pass filter. Both beams were then focused onto the sample such that the pump:probe beam area is roughly 4:1. The probe beam was collected in both transmission and reflection by a biased InGaAs photodiode connected to a lock-in amplifier which is locked to the laser repetition rate. The signal at the lock-in amplifier, as well as the z-position of the stage, was collected by custom software.

6. THEORETICAL MODELING

Using the linear properties of the AZO and fused silica substrate, the absorption of the transmitted (i.e. $T_{AZO} = 1 - R_{AZO}$) pump photon fluence per unit distance into the material is calculated, providing the excess carrier density induced by the incident optical pulse. The incident excitation pulse was considered to have a symmetric a two dimensional Gaussian profile with $1/e^2$ width as determined from beam waist measurements. The induced excess carrier density was then averaged over the thickness of the material for each position x,y and treated as a uniform effective medium which varied in two-dimensions (i.e. the carrier density varies with a Gaussian profile in both x,y directions, which are parallel to the surface of the AZO, and is averaged in z). The temporal response of the system was modeled through the well-known dynamics of pump-probe experiments [36]:

$$f(t) = A_1 \exp\left(\frac{-t}{\tau_1}\right)\left[1 - erf\left(\frac{w}{2\tau_1} - \frac{t}{w}\right)\right] \qquad \textbf{(S2)}$$

where A1 is the amplitude of the process defined by the generation of excess carriers, $\tau 1$ is the recombination time of the excess carriers, and w is cross-correlation width of the pump and probe pulses related the full-width at half-maximum of the Gaussian pulse by $w = 1/\sqrt{2\ln 2}\,\tau_{FWHM}$. This can be further extended to account for multiple decay processes by summing several iterations of Eq. (S2) with varying amplitudes and decay times. For our purposes only one term was required. Once the z-averaged density of the excited carriers was determined for the initial pumping case, the entire distribution was multiplied by Eq. (S2) to determine the change in the carrier concentration in time. Fig. S5 illustrates a 2-D plot of the z-averaged carrier density in time where the y axis is the position along the surface of the sample and the x-axis is time. The peak in excess carrier density here corresponds to point in time of the maximal change in the reflection and transmission.

Using the Drude model, which captures the optical response of the quasi-free excited carriers, the change in the optical properties was determined by adding the contribution of the excess electrons to the un-pumped (intrinsic) permittivity. The loss term in the Drude model was calculated based on mobility in the film as determined from Hall measurements. Following, the transfer matrix approach was used to determine the linear reflection and transmission of the thin film multilayer sample for both the pumped and un-pumped case as a function of the position and time. The results are reported as the percent change in relation to the un-pumped case which was taken as $\Delta R/R_o$, and likewise for transmission. Subsequently, the percent change in the reflection and transmission was multiplied by the probe beam Gaussian profile to account for the spatial overlap of the two beams, and averaged over the $1/e^2$ width of the probe to better approximate the measured signal. Finally, the change in the reflection and transmission was determined in time.

The calculated change in reflection and transmission was matched to experiments through a series of steps. First, the pulse width of our laser is ~120 fs which dictates the rise time of the process. Due to experimental error in recording the absolute z-position of the
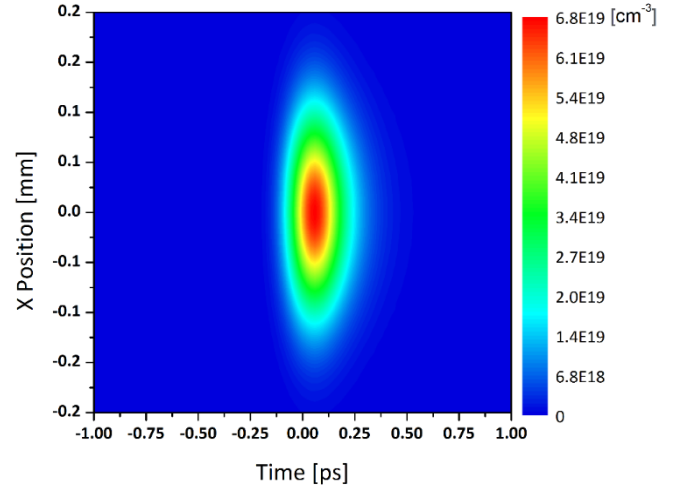

Fig. S5. 2-D plot illustrating the excess carrier distribution in spatial coordinate x (parallel to the sample's surface) and in time for the 350 nm AZO sample under a fluence of 3.9 mJ/cm^2. The maximum induced carrier density corresponds to the maximal change in the reflection and transmission.

computer controlled stage (i.e. delay time), the entire experimental trace is then shifted in time to overlap with the rise time of the laser fitted curve – taking special consideration to overlap points for t < 0 where the response is almost entirely dictated by the pump probe cross-correlation. Secondly, the decay time of the transient is adjusted to match the exponential decay of the experiment, focusing solely on the reflection measurement. The amplitude of the transient is determined by the fluence used during experiment and was only slightly adjusted at the end of the fitting to improve the results. All adjustments made to the incident fluence are within the experimental error, generally < 10% modification.

REFERENCES

1. A. V. Krasavin, A. V. Zayats, and N. I. Zheludev, "Active control of surface plasmon-polariton waves," J. Opt. A-Pure Appl. Op. **7** S85-S89 (2005).
2. A. V. Krasavin, T. P. Vo, W. Dickson, P. M. Bolger, and A. V. Zayats, "All-plasmonic modulation via stimulated emission of copropagating surface plasmon polaritons on a substrate with gain," Nano Lett. **11**(6), 2231-2235 (2011).
3. K. MacDonald, Z. Sámson, M. Stockman, and N. Zheludev, "Ultrafast active plasmonics," Nature Photon. **3**(1), 55-58 (2008).
4. V. J. Sorger, N. D. Lanzillotti-Kimura, R. Ma, and X. Zhang, "Ultra-compact silicon nanophotonic modulator with broadband response," Nanophoton. **1**(1), 17-22 (2012).
5. H. Chen, R. J. Lamond, S. K. Pickus, L. Zhuo Ran, and V. J. Sorger, "A sub-lambda-size modulator beyond the efficiency-loss limit," IEEE Photon. J. **5**(4), 2202411-2202411 (2013).
6. V. Babicheva, N. Kinsey, G. V. Naik, M. Ferrera, A. V. Lavrinenko, V. M. Shalaev, and A. Boltasseva, "Towards CMOS-compatible nanophotonics: ultra-compact modulators using alternative plasmonic materials," Opt. Express **21**(22), 27326-27337 (2013).
7. V. E. Babicheva, R. Malureanu, and A. V. Lavrinenko, "Plasmonic finite-thickness metal–semiconductor–metal waveguide as ultra-compact modulator," Phot. Nano. Fund. Appl. **11**(4), 323-334 (2013).
8. S. Zhu, G. Q. Lo, and D. L. Kwong, "Phase modulation in horizontal metal-insulator-silicon-insulator-metal plasmonic waveguides," Opt. Express **21**(7), 8320-8330 (2013).
9. A. Melikyan, L. Alloatti, A. Muslija, D. Hillerkuss, P. C. Schindler, J. Li, R. Palmer, D. Korn, S. Muehlbrandt, D. van Thourhout, B. Chen, R. Dinu, M. Sommer, C. Koos, M. Kohl, W. Freude, and J. Leuthold, "High-speed plasmonic phase modulators," Nature Photon. **8** 229-233 (2014).
10. A. Melikyan, N. Lindenmann, S. Walheim, P. M. Leufke, S. Ulrich, J. Ye, P. Vincze, H. Hahn, T. Schimmel, C. Koos, W. Freude, and J. Leuthold,

"Surface plasmon polairton absorption modulator," Opt. Express **19**(9), 8855-8869 (2011).

11. K. L. Hall, and K. A. Rauschenbach, "100-Gbit/s bitwise logic," Opt. Lett. **23**(16), 1271-1273 (1998).

12. K. L. Hall, J. Mark, E. P. Ippen, and G. Eisenstein, "Femtosecond gain dynamics in InGaAsP optical amplifiers," Appl. Phys. Lett. **56** 1740-1742 (1990).

13. K. L. Hall, A. M. Darwish, E. P. Ippen, U. Koren, and G. Raybon, "Femtosecond index nonlinearities in InGaAsP optical amplifiers," Appl. Phys. Lett. **62** 1320-1322 (1993).

14. S. Nakamura, Y. Ueno, and K. Tajima, "Femtosecond switching with semiconductor-optical-amplifier-based symmetric Mach-Zehnder-type all-optical switch," Appl. Phys. Lett. **78** 3929-3931 (2001).

15. L. A. Sweatlock, and K. Diest, "Vanadium dioxide based plasmonic modulators," Opt. Express **20**(8), 8700-8709 (2012).

16. K. J. A. Ooi, P. Bai, and H. S. Chu, "Ultracompact vanadium dioxide dual-mode plasmonic waveguide electroabsorption modulator," Nanophoton. **2**(1), 13-19 (2013).

17. J. Gosciniak, S. I. Bozhevolnyi, T. B. Andersen, V. S. Volkov, J. Kjelstrup-Hansen, L. Markey, and A. Dereux, "Thermo-optic control of dielectric-loaded plasmonic waveguide components," Opt. Express **18**(2), 1207-1216 (2010).

18. M. R. Watts, W. A. Zortman, D. C. Trotter, R. W. Young, and A. L. Lentine, "Vertical junction silicon microdisk modulators and switches," Opt. Express **19**(22), 21989-22003 (2011).

19. A. Xu, B. Schmidt, S. Pradhan, and M. Lipson, "Micrometre-scale silicon electro-optic modulator," Nature **435** 325-327 (2005).

20. J. A. Dionne, K. Diest, L. A. Sweatlock, and H. A. Atwater, "PlasMOStor: A metal-oxide-si field effect plasmonic modulator," Nano Lett. **9**(2), 897-902 (2009).

21. N. Kinsey, M. Ferrera, V. M. Shalaev, and A. Boltasseva, "Examining nanophotonics for integrated hybrid systems: a review of plasmonic interconnects and modulators using traditional and alternative materials [Invited]," J. Opt. Soc. Am. B **32**(1), 121-142 (2015).

22. M. Abb, B. Sepulveda, H. M. H. Chong, and O. L. Muskens, "Transparent conducting oxides for active hybrid metamaterial devices," J. Opt. **14**(11), 114007 (2012).

23. D. B. Tice, S. Q. Li, M. Tagliazucchi, D. B. Buchholz, E. A. Weiss, and R. P. H. Chang, "Ultrafast Modulation of the Plasma Frequency of Vertically Aligned Indium Tin Oxide Rods," Nano Lett. **14**(3), 1120-1126 (2014).

24. M. Abb, P. Albella, J. Aizpurua, and O. L. Muskens, "All-optical control of a single plasmonic nanoantenna-ITO hybrid," Nano Lett. **11**(6), 2457-2463 (2011).

25. K. Shi, R. R. Haque, B. Zhao, R. Zhao, and Z. Lu, "Broadband electro-optical modulator based on transparent conducting oxide," Opt. Lett. **39**(17), 4978-4981 (2014).

26. V. E. Babicheva, and A. V. Lavrinenko, "Plasmonic modulator optimized by patterning of active layer and tuning permittivity," Opt. Commun. **285**(24), (2012).

27. V. E. Babicheva, A. Boltasseva, and A. V. Lavrinenko, "Transparent Conducting Oxides for Electro-Optical Plasmonic Modulators," Nanophoton. **In Press** (2015).

28. N. Kinsey, M. Ferrera, G. V. Naik, V. E. Babicheva, V. M. Shalaev, and A. Boltasseva, "Experimental demonstration of titanium nitride plasmonic interconnects," Opt. Express **22**(10), 12238-12247 (2014).

29. R. F. Oulton, V. J. Sorger, D. A. Genov, D. F. P. Pile, and X. Zhang, "A hybrid plasmonic waveguide for subwavelength confinement and long-range propagation," Nature Photon. **2**(8), 496-500 (2008).

30. M. P. Nielsen, and A. Y. Elezzabi, "Ultrafast all-optical modulation in a silicon nanoplasmonic resonator," Opt. Express **21**(17), 20274-20279 (2013).

31. A. V. Krasavin, and N. I. Zheludev, "Active plasmonics: Controlling signals in Au/Ga waveguide using nanoscale structural transformations," Appl. Phys. Lett. **84** 1416-1418 (2004).

32. J. N. Caspers, N. Rotenberg, and H. M. van Driel, "Ultrafast silicon-based active plasmonics at telecom wavelengths," Opt. Express **18**(19), 19761-19769 (2010).

33. R. A. Pala, K. T. Shimizu, N. a. Melosh, and M. L. Brongersma, "A nonvolatile plasmonic switch employing photochromic molecules," Nano Lett. **8** 1506-1510 (2008).

34. G. V. Naik, J. Liu, A. V. Kildishev, V. M. Shalaev, and A. Boltasseva, "Demonstration of Al:ZnO as a plasmonic component for near-infrared metamaterials," Proc. Natl. Academ. Sci. USA **109** 8834-8838 (2012).

35. G. V. Naik, J. L. Schroeder, X. Ni, A. V. Kildishev, T. D. Sands, and A. Boltasseva, "Titanium nitride as a plasmonic material for visible and near-infrared wavelengths," Opt. Mater. Express **2**(4), 478-489 (2012).

36. R. P. Prasankumar, and A. J. Taylor, *Optical Techniques for Solid-State Materials Characterization* (CRC Press, 2012).